npj | clean water

www.nature.com/npjcleanwater

ARTICLE OPEN

Check for updates

# Sustainable and green polylactic acid-based membrane embedded with self-assembled positively charged f-MWCNTs/GO nanohybrids for the removal of nutrients from wastewater

Lobna Nassar[1,2], Vijay S. Wadi[1,3], Hanaa M. Hegab[1,3], Hiyam Khalil[1,2], Fawzi Banat[1,3], Vincenzo Naddeo[4] and Shadi W. Hasan[1,3]✉

In this study, the synthesis, and chemical-physical characterization of self-assembled positively charged multi-walled carbon nanotubes/graphene oxide (f-MWCNTs)/(GO)-nanohybrids into adsorptive PLA-based membranes were investigated. The application of the innovative PLA/f-MWCNTs/GO membrane was investigated for the removal of nutrients such as nitrogen (N) and phosphorus (P) from both synthetic and real wastewater by performing various characterization and performance tests. The positively charged nanohybrid was prepared by electrostatic self-assembly of positively charged f-MWCNTs and negatively charged GO. The amount of nanohybrid loading in the nanocomposite membranes varied from 0 to 6 wt%, and its effects on nutrient removal and water flux were investigated. It is demonstrated that with the addition of only 1.5 wt% f-MWCNT/GO nanohybrid into the PLA matrix, the water flux increased by 74% when compared to the unmodified membrane. Also, up to 90.1 ± 3.4% and 71.3 ± 3.1% removal rates of ammonium-nitrogen ($NH_4^+$-N) and phosphate ($PO_4^{3-}$-P) ions were achieved using raw wastewater, respectively. The obtained results confirm the practical usability of the proposed innovative material for membrane fabrication in real wastewater treatment applications and can open doors to efficient and sustainable methods for nutrient removal.

*npj Clean Water* (2022)5:57 ; https://doi.org/10.1038/s41545-022-00206-w

## INTRODUCTION

The high accumulation of nutrients, including nitrogen (N) and phosphorus (P), discharged into surface water, rivers, and reservoirs can accelerate eutrophication and cause great damage to the aquatic ecosystem, i.e. fish toxicity and depletion of dissolved oxygen[1,2]. Therefore, controlling N and P levels in the surface water is essential to inhibit the occurrence of eutrophication. Thus, the development of innovative technologies for the treatment of nutrients is highly needed[3,4].

Several treatment technologies are used to remove nutrients from wastewater. These include chemical oxidation, coagulation/flocculation, adsorption, biological processes (anaerobic/aerobic), and combustion[5,6], among others[7,8]. Typically, N can be chemically removed through several methods, such as chlorination or nitrification processes[9]. Although this approach is very effective in removing excess ammonia ($NH_3$), it is not sensitive to temperature discrepancies, in addition to the formation of undesirable by-products in drinking water and causing a serious threat to the aquatic biota[10,11]. Alternatively, biological treatment approaches often take a long time to reduce the concentration of $NH_3$ and its efficiency is not encouraging at elevated $NH_3$[12]. Similarly, the elimination of P from wastewater is mainly achieved by chemical or biological approaches. Nevertheless, such methods are incapable of offering additional purification. Although the chemical precipitation process results in low levels of P in the effluent, it generates a big amount of difficult-to-handle chemical sludge, which also causes secondary contamination to the environment[13,14].

Recently, membrane technology has become the focus of research to investigate its efficiency in the removal of $NH_3$, as it has great potential and high efficiency to replace conventional $NH_3$ removal processes[15,16]. Accordingly, several studies on the applications of membranes in $NH_3$ removal were reported. However, insufficient studies have been conducted on this topic, and more detailed investigations are needed. Moreover, it was reported that adsorptive flat-sheet membranes, combining the advantages of membrane purification with the adsorption method, effectively remove $NH_3$ from wastewater. A key component of adsorption-based membranes is the active functional groups that scavenge $NH_3$ either by ion exchange or surface complexation[17]. Materials such as zeolite and gypsum have been extensively described to trap $NH_3$ from wastewater and have been recognized as potentially efficient adsorption materials due to their large ion exchange power for the elimination of $NH_3$[18,19]. The main obstacle with these materials is their rapid degradation in water. Moreover, during the process, various elements and ions may leach into the solution, which could affect the final performance of the adsorbent to remove $NH_3$[11]. Rohani et al. reported the successful integration of zeolite and gypsum with a polyvinylidene fluoride (PVDF) flat sheet membrane for the effective removal of $NH_3$[20].

Adsorption is also a potential option to obtain low P discharge during the treatment of diluted waters. Lanthanide-based nanomaterials are often considered effective and favorable materials for P removal[21]. However, these adsorbents can easily aggregate due to their high surface energy, thus, reducing their productivity[22]. Integrating Lanthanide-based nanomaterials with the supporting substrates to obtain dispersibility and high adsorption ability can provide a possible route to overcome these obstacles[23]. In two different studies,

[1]Center for Membranes and Advanced Water Technology (CMAT), Khalifa University of Science and Technology, PO Box 127788, Abu Dhabi, United Arab Emirates. [2]Department of Civil Infrastructure and Environmental Engineering, Khalifa University of Science and Technology, PO Box 127788, Abu Dhabi, United Arab Emirates. [3]Department of Chemical Engineering, Khalifa University of Science and Technology, PO Box 127788, Abu Dhabi, United Arab Emirates. [4]Sanitary Environmental Engineering Division (SEED), Department of Civil Engineering, University of Salerno - Via Giovanni Paolo II #132, 84084 Fisciano (SA), Italy. ✉email: shadi.hasan@ku.ac.ae

lanthanum (La) was used to modify PVDF and polyacrylonitrile (PAN) substrates to fabricate composite membranes with simultaneous adsorption/filtration functions capable of removing P from wastewater[2,24].

Among the nano adsorbents used in wastewater treatment applications, graphene oxide (GO) and carbon nanotubes (CNTs) have been reported in the literature. Researchers have incorporated these materials in polymeric membranes and have proved to enhance the membrane's properties, due to their desired mechanical and physical properties as well as unique nanostructure. Research findings revealed that MWCNTs increase membranes tensile strength significantly[25] and functionalized CNTs (f-CNTs) outperformed the neat membrane in terms of $NH_3$ removal, flux, and hydrophilicity[26]. The improved $NH_3$ removal using f-CNTs is ascribed to $NH_3$ adsorption on the active functional groups of the f-CNTs[26]. Furthermore, GO surface-modified membranes showed higher water flux, hydrophilicity, and better antifouling properties[27,28]. Moreover, the addition of GO in polymeric membranes have proved to significantly enhance the thermal stability, tensile strength, and antibacterial properties of the membrane[29,30].

However, studies are very limited when it comes to GO and CNT being used together as one nanohybrid. CNT/GO nanocomposite was introduced into polyelectrolyte complex (PEC)[31] and polydimethylsiloxane (PDMS)[32] for the fabrication of pervaporation membranes. The two studies concluded that due to the introduction of the three-dimensional network constructed by CNT and GO; CNT/GO membranes showed improved mechanical strength, separation performance, and operation stability compared to that of CNTs and GO nanocomposite membranes. Additionally, CNT/GO nanocomposites have also proved to enhance thermal decomposition[33].

Biopolymers have been studied as promising materials for the fabrication of green and biodegradable separation membranes[34]. Recently, polylactic acid (PLA) has gained great attention as a significant recyclable, biodegradable, and sustainable polymeric material[35]. In one study, PLA membranes integrated with metal oxides have shown outstanding performance in terms of high flux and perfect oil/water mixture seperation[36]. Furthermore, PLA membranes were reported to remove 99% of bacterial cells in a different study[37] and up to 92% of BSA, as well as revealing high antifouling properties in another study[38].

After a comprehensive and up-to-date overview of the literature, our research group is the first to report the fabrication of PLA membranes for the removal of nutrients from synthetic and real wastewater. Unlike synthetic polymers, PLA was chosen for such an application because of its low toxicity and recyclability. The PLA membrane with 20 wt% removed ~96 and ~87% of $NH_4^+$-N and ~22 and ~52% of $PO_4^{3-}$-P using synthetic and raw wastewater, respectively. However, water permeability was found to decrease significantly as the polymer content increased[39]. Therefore, this study aimed to continue our previous efforts via fabricating nanohybrid-based adsorption membranes from PLA and functionalized positively charged multi-walled carbon nanotube/graphene oxide/nanohybrids in a PLA (i.e., f-MWCNTs/GO) membrane, which can simultaneously remove $NH_3$ and P from wastewater while enhancing water permeability. An in-depth investigation was conducted to analyze the efficiency of the fabricated membranes in removing the tested nutrients in terms of water flux and removal capacity, in addition to morphological, thermal, wettability, and chemical studies by scanning electron microscopy (SEM), energy-dispersive X-ray spectroscopy (EDS), X-ray diffraction (XRD), thermogravimetric analyzer (TGA), contact angle (CA), and Fourier transform infrared spectroscopy (FTIR).

## RESULTS AND DISCUSSION

### f-MWCNTs/GO nanohybrid characterization

The SEM images of MWCNTs, MWCNTs-COOH, f-MWCNTs, graphite (Gt), GO nanosheets, and f-MWCNTs/GO nanohybrid are shown in Fig. 1a. It was observed that pristine MWCNTs were tangled with each other and displayed a high tendency to form bundles due to strong Van der Waals forces[40,41]. Moreover, the surface is much smoother compared to the surface of MWCNTs-COOH and f-MWCNTs. Furthermore, the SEM images of MWCNTs-COOH and f-MWCNTs verified the presence of a more open small bundle and shorter tube length due to the strong acidic treatment and functionalization[42]. As seen in Fig. 1a, the Gt sheets are compact lamellar structures composed of stacked alternating layers with well-defined sharp edges. However, the GO sheets displayed smooth crumpled wave-like surface morphology and the sheets are randomly arranged, which could be attributed to the increased interlayer *d*-spacing during the oxidation process. The XRD patterns of the pristine Gt and GO (Fig. 1e) further confirmed that the interlayer *d*-spacing became wider. The SEM image of the f-MWCNTs/GO nanohybrid shows that the f-MWCNTs and GO are stacked together due to the strong electrostatic interaction between positively functionalized f-MWCNTs and negative GO. Similar surface morphologies have also been reported in the literature[42–46]. The oxidation of MWCNTs to MWCNTs-COOH displayed a negative zeta potential of $-35.1 \pm 1.9$ mV due to the presence of C=O, -COC, -OH groups (Fig. 1b)[45]. Similar negative functional groups were also present in the GO nanosheets[46]; which can be attributed to a negative net charge of $-45.1 \pm 2.5$ mV. While, after functionalization, the net charge on the f-MWCNTs changed to positive $63.2 \pm 2.7$ mV, which further confirms the functionalization and protonation of $NH_3^+$.

The objective of this study was to synthesize multifunctional membranes as the targeted pollutants are charged oppositely. The polymer, PLA, used is highly negative, having a potential zeta potential value of ~−25 mV[47] at a pH of 7; therefore, a positively charged nanohybrid was required to increase the functionalities of the membranes. The positively charged self-assembled nanohybrids were synthesized using different ratios of f-MWCNTs and GO, including 60:40, 70:30, and 80:20, and tested for their zeta potential. The prepared ratio of 80:20 of f-MWCNTs to GO had the highest net positive charge of $27.1 \pm 1.0$ mV (Fig. 1b); therefore, it was selected to be incorporated into the membranes.

The TGA weight loss curves of the fabricated nanomaterials are shown in Fig. 1c. The pristine MWCNTs showed good thermal stability up to 550 °C, with approximately 10% weight loss, related to the traces of carboxylic acid groups or moisture that was generated during purification. After further heating, the MWCNTs showed a sharp degradation to 700 °C with a final weight loss of 93%. The MWCNTs-COOH showed a three-step thermal decomposition due to the presence of carboxylic functional groups. The first major decomposition results in a 31% weight loss between 54 and 200 °C, which is attributed to the loss of adsorbed moisture or solvent, followed by a second major decomposition between 200 and 300 °C (≈24% loss) due to the less thermally stable oxygen-containing functional groups. Lastly, an additional 36% weight loss between 400 and 700 °C was observed due to the combustion of the carbon skeleton. The functionalization of MWCNTs resulted in a more thermally stable structure than MWCNTs-COOH, losing only 25% of its weight up to 500 °C, which is attributed to the presence of amino groups[48]. For the thermal decomposition of GO, which occurred over three stages: the weight loss below 100 °C is attributable to the evaporation of any moisture or solvent (≈17% loss); from 140 to 242 °C which is due to the decomposition of oxygen groups and carbon oxidation (≈28% loss); and finally, the complete decomposition which is observed from 500 to 600 °C (≈35% loss)[49]. The pristine Gt exhibited 0% weight loss up to 700 °C. The f-MWCNTs/GO nanohybrid displayed thermal

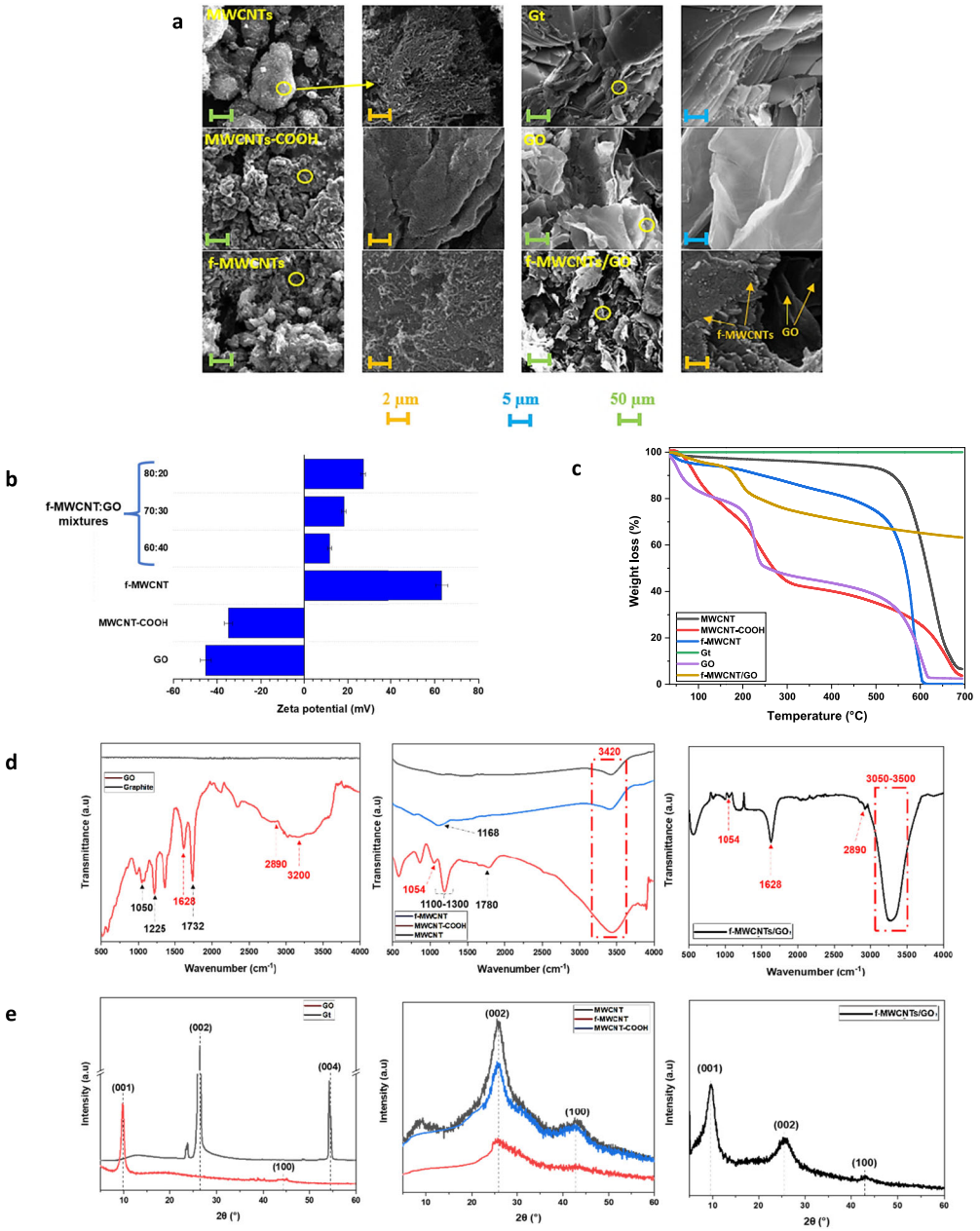


**Fig. 1 Nanomaterial characterization.** **a** SEM images of prepared nanomaterials. **b** Zeta potential measurements of the fabricated nanohybrids with different ratios. **c** TGA curves of the fabricated nanomaterials. **d** FTIR spectrum of fabricated nanomaterials. **e** XRD patterns of fabricated nanomaterials.

stability and its thermal degradation occurred through two gradual decomposition stages, one over the temperature between 50 and 200 °C (≈15% loss) and another from 235 °C to 700 °C, with only 17% weight loss.

FTIR and XRD analyses were carried out to confirm the successful preparation and functionalization of nanomaterials as illustrated in (Fig. 1d, e). According to Fig. 1d (left), no significant peaks were observed in the Gt spectrum, while the GO spectrum reveals several functional groups. The GO absorption peaks appeared at 1050, 1225, 1628, 1732, 2890, and 3200 $cm^{-1}$, which are attributed to the presence of C-O of the alkoxy group, C-O of the epoxy group, C=C, -C=O, symmetric and asymmetric -$CH_2$- and -OH (in the -COOH group) stretching vibrations, respectively[43,50,51]. These peaks confirmed the successful oxidation of Gt. Figure 1d (center) shows the FTIR spectra of MWCNTs, MWCNTs-COOH, and f-MWCNTs. The pristine MWCNTs showed a weak peak of -OH vibration at 3420 $cm^{-1}$, due to the partial oxidation of the MWCNTs during purification[44]. Furthermore, the presence of a new peak at 1168 $cm^{-1}$, attributed to the stretching vibration of C-O, as well as the increased intensity of the -OH group after oxidation, proves the successful synthesis of MWCNTs-COOH. The spectrum of f-MWCNTs verified the successful functionalization of MWCNTs through the existence of new characteristic peaks, including 1054, 1100–1300, and 1780 $cm^{-1}$, corresponding to the stretching vibrations of C-N, C-H, and C=O. In addition, the broadband centered at 3420 $cm^{-1}$ represents the overlap of -OH and amino groups[48,52–54]. Due to the introduction of all these groups on the surface of MWCNTs, oxidized and amino-functionalized MWCNTs would produce much higher sorption capacity and sites[55]. Subsequently, the f-MWCNTs/GO nanohybrid exhibited peaks

found in both f-MWCNTs and GO nanomaterials, which confirms the successful formation of a self-assembled nanohybrid.

XRD cellular units (*d*-spacing) were performed to identify the structure of the prepared nanohybrids. The XRD patterns of Gt and GO are demonstrated in Fig. 1e (left). The Gt shows two sharp and intense peaks at $2\theta = 26.5°$ and 54.5° for the planes (002) and (004) with *d*-spacing of 3.4 and 1.7 Å, respectively, indicating the typical crystal structure of Gt. The GO XRD pattern shows a diffraction characteristic peak (001) at $2\theta = 9.9°$ with the *d*-spacing of 8.9 Å between the nanosheets, confirming the successful synthesis of GO[56]. The increase in *d*-spacing between the GO nanosheets is attributed to the presence of bulky oxygen functional groups[57,58]. Figure 1e (center) illustrates the XRD patterns of the different MWCNTs, MWCNTs-COOH, and f-MWCNTs. The strong diffraction peak at $2\theta = 26°$ can be indexed as the (002) reflection of the hexagonal Gt structure with a *d*-spacing of 3.4 Å. The peak around 43° has a *d*-spacing of 2.1 Å and is due to the (100) graphitic planes[59]. All three MWCNTs have the same diffraction peaks; however, the pristine MWCNTs have the highest intensity while the f-MWCNTs has the lowest, suggesting that the semicrystalline structure of pristine MWCNTs slightly changed corresponding to their oxidation and functionalization, respectively. Finally, Fig. 1e (right) shows the XRD patterns of the f-MWCNTs/GO nanohybrid with a diffraction peak at 9.5°. This could be derived from GO; however, it had a wider *d*-spacing of 9.3 Å, compared to the GO *d*-spacing of 8.9 Å. Furthermore, two additional peaks were observed at $2\theta = 26°$ and 43°, which were derived from the Gt-like structure of MWCNTs[60,61]. The XRD patterns suggest that the f-MWCNT/GO nanohybrid increases the structural heterogeneity and the interlayer distance compared to GO or f-MWCNT individually due to the formation of a self-assembled structure.

### Nanocomposite membranes characterization

Multiple sorts of linkages may be attributed to the interaction between the f-MWCNTs/GO nanohybrid and the PLA membrane matrix. Since the f-MWCNTs/GO nanohybrid and the PLA polymer share the same hexatomic ring of carbon atoms, the π–π interactions stack them spontaneously[62]. Furthermore, electrostatic and/or ion-pair interactions occur between the positively charged f-MWCNTs/GO nanohybrid and the hydroxyl groups of PLA. Additionally, the PLA's -OH groups tend to create hydrogen bonds with the amide groups of f-MWCNTs' surface functional groups. These interactions increased the stability of the f-MWCNTs/GO nanohybrid in the composite membranes significantly. This was validated by a leaching experiment in which composite membranes were immersed in DI water for 72 h while being vigorously shaken[63]. To calculate the percentage of leached nanomaterial, the mass difference before and after immersing the membrane was recorded. There was no leaching, which supports the long-term operation of PLA/f-MWCNTs/GO composite membranes due to their excellent characteristics.

EDS elemental mapping of the C, O, and N was carried out on the fabricated membranes to confirm the successful incorporation of the f-MWCNT/GO nanohybrid within their structure. The results demonstrated in Fig. 2a indicated that both PLA and the nanohybrids showed C and O in all samples; however, the presence of N in the nanocomposites was attributed to the incorporation of amine groups from the f-MWCNTs/GO nanohybrids. From both visual observation (Supplementary Fig. 3) and the dispersion of N in the membranes, it can be concluded that the nanohybrid is evenly distributed in the composite membranes.

Surface SEM images of PLA membranes prepared with different f-MWCNTs/GO nanohybrid are shown in Fig. 2b. SEM images of all membranes showed a porous structure; however, as the concentration of nanocomposite increases, the porosity decreases, the pore size increases, and the surface of the membrane become rough. Similar observations were also previously reported[64]. The increase in pore size can be associated with the hydrophilic nature of the nanohybrid f-MWCNTs/GO, during the non-solvent induced phase separation (NIPS) process, the hydrophilic nanomaterials generate more water penetration sites into the membranes, hence creating an open structure membrane that is more porous[65,66]. On the other hand, porosity decreased due to the increase in the dope solution's viscosity when the nanohybrid content increased, which affected the exchange rate between the non-solvent (DI water) and the N-Dimethylacetamide (DMAc) solvent and led to slower phase separation during the NIPS process[67]. This resulted in the suppression of the finger-like sublayer and the formation of wider microvoids in the M6 membrane, compared to the pristine membranes (Fig. 2a). The hydrophilicity and viscosity nature of the dope solution controls the final membrane structure[68,69].

The presence of f-MWCNTs/GO nanohybrid in the PLA polymer matrix was verified via FTIR and TGA. First, the thermogravimetric analyzer (TGA) analysis was performed to examine the thermal stability of the membranes. It was found that as the content of f-MWCNT/GO nanohybrids increased, the thermal stability of the membranes also increased (Fig. 2c). The composite membranes M1.5, M3, and M6 demonstrated thermal degradation ($T_d$) at almost 300, 321, and 331 °C, respectively, which were all higher, compared to the pristine membrane degradation temperature of 284 °C. This was due to the strong interactions between the PLA polymer chains and the nanohybrid. A similar trend was obtained in the literature, indicating that the addition of MWCNTs or GO within the PLA membrane matrix enhanced its thermal stability[25,30].

Lastly, FTIR analysis was carried out to investigate the surface functional groups of the pristine PLA and nanocomposite membranes (Fig. 2d). PLA showed peaks at 1100, 1454, and 1754 $cm^{-1}$, which were related to the -C-O, C-H in $CH_3$ and -C=O, respectively[70]. Additional PLA peaks were observed at 2947 and 2997 $cm^{-1}$, which corresponded to the C-H asymmetric stretching vibration[30] and 1690 $cm^{-1}$ peak, which corresponded to the carbonyl absorption of PVP[71]. Finally, the peaks that are attributed to the nanocomposite were observed at 1429 and 1676 $cm^{-1}$ and corresponded to the CO-NH- and C-N stretching vibrations, respectively[72]. The intensity of these two peaks was noticed to increase and became sharper as the nanohybrid content increased in the composite membranes.

### Influence of f-MWCNTs/GO nanohybrid on membrane's performance

The porosity and mean pore size were calculated (Supplementary Fig. 4). In addition, the static (Fig. 3a) and dynamic (Supplementary Fig. 5) DI water CAs of all membranes were measured to evaluate their hydrophilicity. The CAs of all membranes decreased with an increase in the nanohybrid loading over time. The pristine membrane had the highest CA value, while the M6 membrane had the lowest CA value of $70.2 \pm 2.1°$ and $58.8 \pm 2.1°$, respectively. A similar CA value of the pristine PLA membrane was reported in the literature[73]. The wettability of nanocomposite membranes was enhanced compared to that of pristine membranes, due to the presence of hydrophilic functional groups of GO and f-MWCNTs, such as -OH and carboxyl groups, in addition to amino groups in the f-MWCNTs[74]. Furthermore, the functionalization of MWCNTs leads to their hydrophilic moieties being highly distributed within the membrane polymer matrix[64].

However, the surface free energy of the membranes, shown in Fig. 3a, followed an opposite trend to the static DI water CA. The surface free energy of the PLA membranes increased with the increase in the nanocomposite content. For example, the surface free energy of the membranes of P, M1.5, M3, and M6 was $97.7 \pm 1.1$, $101.5 \pm 2.5$, $108.7 \pm 2.1$, and $110.5 \pm 3.1$ mJ $m^{-2}$,

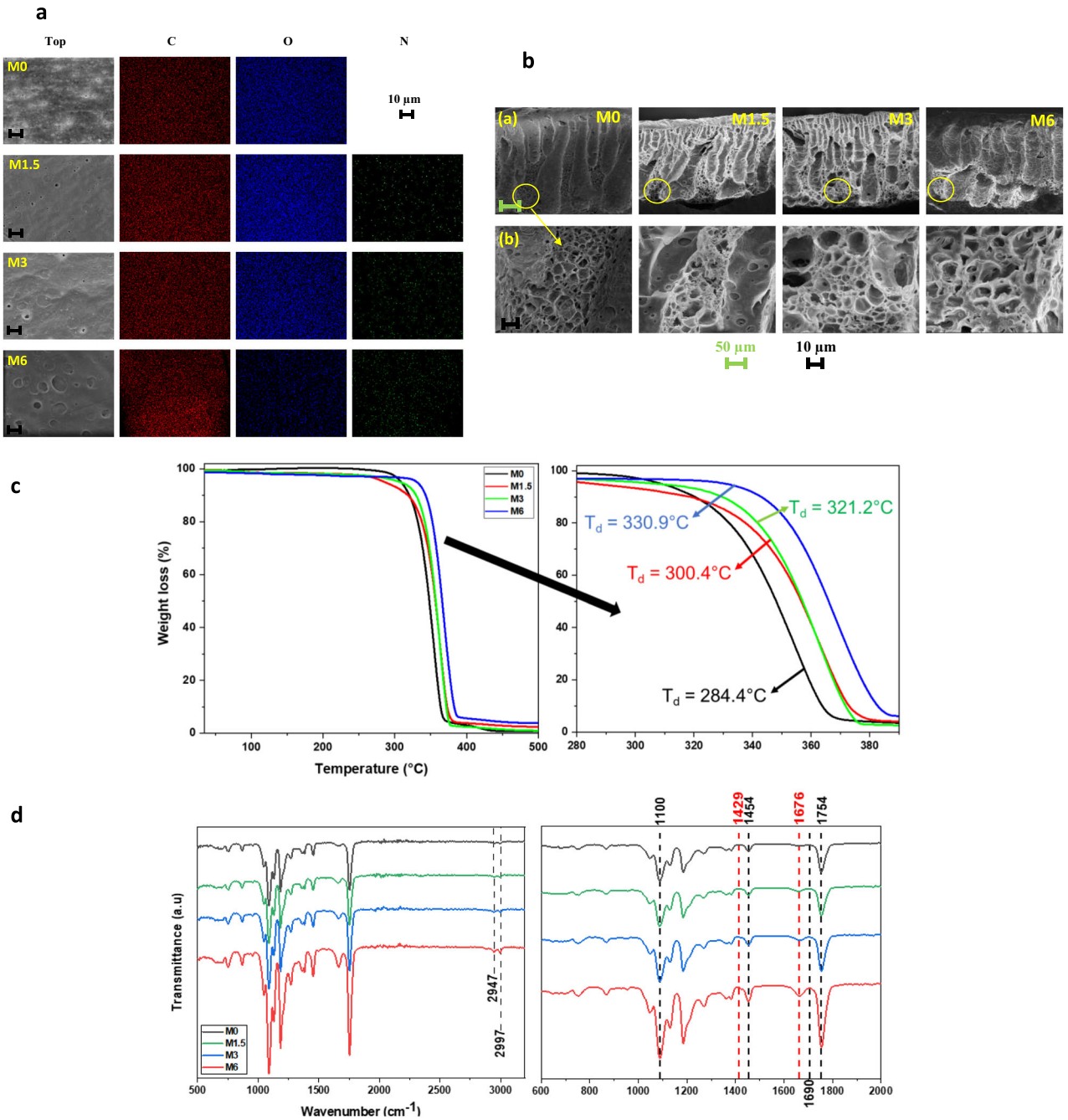


**Fig. 2 Nanocomposite membranes characterization. a** SEM images and EDS elemental mapping of the pristine and nanocomposite membranes. **b** Cross-sectional and magnified SEM images of the pristine and nanocomposite membranes. **c** TGA curves of the pristine and nanocomposite membranes. **d** FTIR spectrum of pristine and nanocomposite membranes.

respectively. In general, both the CA and surface free energy results showed that the nanohybrid's addition improved the membranes' hydrophilicity. This improvement could be positively reflected in the water permeability of the nanocomposite membranes (Fig. 3b). The results revealed that the water permeability of the membranes increased with the increase of the nanohybrid loading. Therefore, the pristine membrane showed the lowest water flux with a value of $24.3 \pm 1.2\ L\ m^{-2}h^{-1}$ and increased tremendously to reach $106.7 \pm 4.2\ L\ m^{-2}h^{-1}$ for the M6 membrane, almost five times better than the pristine membrane. These results are consistent with the mean pore size, porosity (Supplementary Fig. 4), and CA outcomes.

### Synthetic wastewater filtration

The static adsorption of nutrient ions was investigated using fabricated membranes and synthetic wastewater (Supplementary Fig. 6). The results revealed that the static adsorption of $NH_4^+$-N was higher than that of $PO_4^{3-}$-P for all membranes. To further understand the static results obtained, the ζ-potential was investigated at a wide range of pH, from 2.5 to 11.5 for the pristine and M1.5 membranes (Fig. 3c). The ζ-potential of the membranes was around −21 and −14 mV for pristine and M1.5 membranes, respectively, at pH = 7, at which all the analyses in this study were carried out. Similar ζ-potential values of pristine PLA membranes were reported in the literature[39,47].

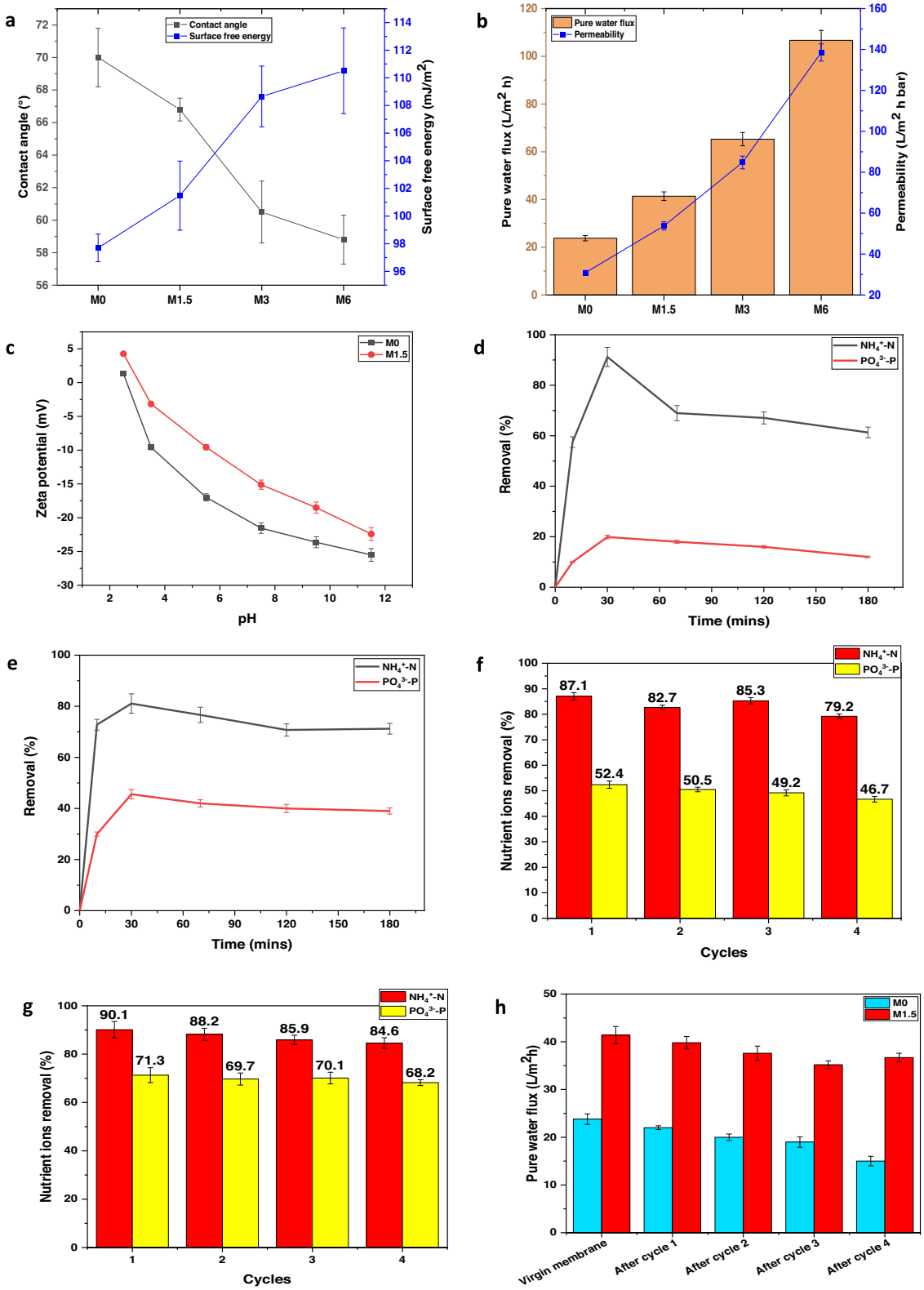


**Fig. 3 Performance of membranes. a** Static CA and surface free energy of the pristine and nanocomposite membranes. **b** Pure water flux and permeability profiles of the pristine and nanocomposite membranes. **c** Zeta potential of M0 and M1.5 membranes. Nutrient ions removal over 3 h of operation using **d** the M0 membrane and **e** the M1.5 membrane. Nutrient ion removal of **f** M0, **g** M1.5 membranes, and **h** pure water flux after several raw wastewater filtration cycles.

As demonstrated, the ζ-potential was significantly affected by the addition of the nanohybrid, the M1.5 membrane's ζ-potential increased due to the positively charged nanohybrid added (Supplementary Fig. 1b and Fig. 1b).

In addition, the dynamic filtration of nutrients removal rate was evaluated. After 30 min of filtration (Supplementary Fig. 7), the dynamic nutrient removal outcomes were consistent with the static adsorption results. It was expected that the membrane with higher adsorption capacity will form a superficial layer of nutrients on its surface and this would positively reflect on the nutrient removal rate based on the repulsion mechanism (Supplementary Fig. 8). The pristine membrane exhibited the highest $NH_4^+$-N ion removal (91.2 ± 5.1%), and decreased slightly with the addition of nanohybrid content. M1, M3, and M6 membranes rejected $NH_4^+$-N ions with rates of 81.3 ± 4.2%, 68.1 ± 3.1%, and 55.2 ± 2.8%. Although $PO_4^{3-}$-P removal rates were enhanced with the addition of nanohybrid content, M1.5, M3, and M6 membranes showed higher rejection rates of 46.3 ± 2.2%, 49.4 ± 2.5 %, and 42.2 ± 2.1%, than the rejection rate of the pristine membrane (20.1 ± 0.7%).

The main separation mechanisms of the $NH_4^+$ and $PO_4^{3-}$ ions of the fabricated membranes are by adsorption/repulsion (Supplementary Fig. 8), which have been proved by the post-filtration characterization tests (Supplementary Figs. 9, 10). In the case of the pristine membrane, $NH_4^+$ ions cannot pass through the pores of the membrane due to the positively charged superficial layer formed on the surface. This layer is formed when $NH_4^+$ ions are attached to the negatively charged surface of the membrane. This leads to the repulsion of $NH_4^+$ ions; thus, reducing the diffusion of $NH_4^+$ ions into the membrane phase. In nanocomposite membranes, the positively charged nanohybrid (Fig. 1b) slightly reduces the adsorption of $NH_4^+$ ions and, consequently the formation of a positively charged superficial layer. This explains the decrease in the removal of $NH_4^+$ ions as the nanohybrid content increased; this trend was observed in several literature studies[20,39,75]. On the contrary, the nanocomposite membranes exhibited a higher rejection of $PO_4^{3-}$ ions than the pristine membrane, due to the higher $PO_4^{3-}$ ions adsorption capacity of the less negative nanocomposite membranes, and the formation of a negative superficial layer is greater. This can also be supported by the ζ-potential measurements (Fig. 3c).

Overall, based on all previous results, all the nanocomposite membranes have higher flux, are more hydrophilic, and have better thermal stability than the pristine membrane. However, the most promising fabricated membrane is M1.5 because it has the highest nutrient removal rates among the other nanocomposite membranes and has doubled the flux of the pristine membrane. Therefore, M1.5 was compared to the pristine membrane in the following analyses.

The performance of M0 and M1.5 membranes, in terms of nutrient ion removal, was assessed for a prolonged filtration experiment for 3 h (Fig. 3d, e). Permeate samples were collected at intervals of 10, 30, 70, 120, and 180 min for analysis. In the first 30 min, the pristine membrane showed higher rejection of $NH_4^+$-N; however, of 91.2 ± 5.1% and then decreased to 61.2 ± 2.1% after 180 min of operation, while the removal rate of $PO_4^{3-}$-P ions was 20.4 ± 0.2% and reduced to 12.1 ± 0.3% over the filtration time. On the other hand, the M1.5 membrane demonstrated a more stable nutrient removal profile. Therefore, its performance decreased only by ≈10 and ≈6% for $NH_4^+$ and $PO_4^{3-}$ ions, respectively. Furthermore, the M1.5 membrane showed a higher rejection of $NH_4^+$-N in the first 10 min of 73.1 ± 2.1%, compared to only 57.2 ± 2.3% of the pristine membrane. A similar trend was observed by He et al., which could be explained as follows: first, rapid adsorption of $NH_4^+$ ions occurs on the exterior surface of the adsorbent until it reaches the saturation point, then $NH_4^+$ ions would start to be adsorbed at the interior surface of the adsorbent[76]. At the start of the experiment, the availability of plenty of free readily adsorption sites leads to a fast diffusion and rapid equilibrium accomplishment; hence, the M1.5 membrane has more adsorption sites on its exterior surface than the pristine membrane, and it has greater prolonged complexation/adsorption of nutrients on its surface. However, the pristine membrane has less adsorption sites since it showed a higher $NH_4^+$-N rejection for only 30 min and then declined. Furthermore, the M1.5 membrane showed a higher overall $PO_4^{3-}$-P rejection of 46.3 ± 2.2%, compared to only 20.1 ± 20.8% when compared to the M0 membrane. Lastly, the slight reduction in nutrient removal after 30 min of filtration for both membranes is due to the saturation of the all-active sites in the membrane.

To further provide useful insights about the adsorption mechanisms, the kinetics of adsorption of membrane M1.5 were studied as a function of time during 180 min. For evaluating the adsorption kinetics of the nutrients, pseudo-first and pseudo-second-order models were applied according to Eqs. (1) and (2), respectively[77].

$$q_t = q_e(1 - e^{-K_1 t}) \tag{1}$$

$$q_t = \frac{K_2 q_e^2 t}{1 + K_2 q_e t} \tag{2}$$

where $q_t$ and $q_e$ (mg g$^{-1}$) represent the adsorption capacity at equilibrium and time t, respectively, and $k_1$ (min$^{-1}$) and $k_2$ (g mg min$^{-1}$) indicate the first- and second-order rate constants, respectively. The obtained parameters of pseudo-first-order and pseudo-second-order kinetics models are given in Supplementary table 2. The results show that both nutrients $q_{exp}$ are closer to the $q_e$ of the second-order kinetics model. In addition, the correlation coefficients of both nutrients for the second-order kinetic model ($R^2 > 0.99$) are much higher than those of the first-order kinetic model, when the experimental data is fitted. This suggests that the second-order kinetics model describes the data better and is more appropriate for the nutrient adsorption process. Previous studies in the literature have also concluded that the second-order kinetic model fits the experimental data better when it comes to nutrient adsorption[78–80].

The experimental data were analyzed using two theoretical isotherm models, Langmuir and Freundlich, expressed by Eqs. (3) and (4)[81], respectively.

$$q_e = \frac{q_{max} K_L C_e}{1 + K_L C_e} \tag{3}$$

$$q_e = K_F C_e^{1/n} \tag{4}$$

where $C_e$ represents the equilibrium adsorbate concentration (mg L$^{-1}$), $q_{max}$ defines the maximum adsorption capacity (mg g$^{-1}$), $K_F$ and n are Freundlich constants, and $K_L$ (L mg$^{-1}$) denotes the Langmuir constant, which is related to the binding sites adsorption affinity. Due to the greater $R^2$ coefficient, the Freundlich model can be a better fit for modeling the adsorption isotherms of both nutrients, as shown in Supplementary Table 3. Furthermore, the high $K_F$ values imply that both nutrients are easily adsorbed.

### Raw municipal wastewater filtration

The reusability of the pristine and M1.5 membranes was evaluated using raw municipal wastewater for four cycles of filtration operation (Fig. 3f, g). Furthermore, to investigate the durability of the membranes, cleaning with only water was performed after each cycle, and the permeate flux of the membranes was recorded (Fig. 3h). The results (Fig. 3f, g) showed that the performance of the M1.5 membrane enhanced using raw wastewater, compared to synthetic wastewater (Supplementary Fig. 7). For example, the rejection of $NH_4^+$ ions was 90.1 ± 3.4% for M1.5 membrane, using raw wastewater, compared to 81.3 ± 4.2% using synthetic

**Table 1.** Compositions of dope solutions used in the fabrication of membranes.

| Label | PLA (wt.%) | PVP (wt.%) | f-MWCNT-GO (wt.%)* | DMAc (wt.%) |
|---|---|---|---|---|
| M0 | 20 | 2 | 0 | 78 |
| M1.5 | 20 | 2 | 1.5 | 78 |
| M3 | 20 | 2 | 3 | 78 |
| M6 | 20 | 2 | 6 | 78 |

*The weight percentage is with respect to the total weight of the PLA used.

wastewater. Similarly, the $PO_4^{3-}$-P rejection increased by 26% using raw wastewater. While in the case of the pristine membrane, the rejection of $NH_4^+$-N was 4% lower and the rejection of $PO_4^{3-}$-P was 32% higher using raw wastewater. Furthermore, the results indicated that the M1.5 membrane maintained higher removal of both nutrients after four cycles of operation. The overall removal of the $NH_4^+$-N and $PO_4^{3-}$-P dropped slightly from 90.1 ± 3.1%, and 71.3 ± 3.2% to 84.6 ± 2.2%, and 68.2 ± 1.3%, respectively. Although the pristine membrane rejection rates of the $NH_4^+$ and $PO_4^{3-}$ ions decreased significantly from 87.1 ± 1.4%, and 52.4 ± 1.4% to 79.2 ± 0.9%, and 46.7 ± 1.1%, respectively. The decline in the rejection rate is related to the rapid saturation with nutrients, resulting in adsorption/leakage or incomplete desorption prior to cleaning the membranes. This was also reflected in the water flux measurements after each cycle (Fig. 3h). Therefore, the water flux of the pristine and M1.5 membranes dropped by ≈36%, and ≈11%, respectively, after four cycles of operation. The superior performance of the M1.5 membrane over the pristine membrane is mainly attributed to the existence of hydrophilic f-MWCNTs/GO nanohybrid, which greatly enhanced the surface morphology and the hydrophilicity of the nanocomposite membranes. This would mitigate the accumulation of contaminants and improve the cleaning process. From these results, it can be concluded that the fabricated f-MWCNTs/GO-based PLA nanocomposite membranes can be regenerated and reused with simple water cleaning while maintaining a high removal rate. The performance of the M1.5 membrane was further compared with that of other membranes targeting the same pollutants studied in the literature (Supplementary Tables 4, 5).

In this study, the self-assembled f-MWCNTs/GO nanohybrid was successfully synthesized and integrated into the PLA mixed matrix membrane for the removal of $NH_4^+$-N and $PO_4^{3-}$-P. The performance of PLA nanocomposite membranes based on f-MWCNTs and GO was significantly improved with the addition of the new nanohybrid in terms of higher water permeability. The fabricated nanocomposite can be used for the simultaneous removal of $NH_4^+$ and $PO_4^{3-}$ ions without the negative impact of the nutrient ions present at the same time, as demonstrated by the use of raw municipal wastewater as feedstock. The fabricated membranes are stable and can be regenerated by simply washing with water; this confirms the applicability of the fabricated membranes in real wastewater applications.

## METHODS

### Synthesis of self-assembled f-MWCNT/GO nanohybrid

The f-MWCNTs and GO nanosheets were prepared by similar methods reported in the literature (Supplementary Fig. 1a, b). The self-assembled positively charged f-MWCNTs/GO nanohybrid (Supplementary Fig. 1c) was prepared via the electrostatic co-precipitation approach. Briefly, the 80:20 f-MWCNT/GO preparation was as follows: 120 mL of GO solution (1.5 mg $mL^{-1}$) was ultrasonicated for 30 min to ensure exfoliation and homogeneous dispersion. In a separate beaker, 480 mL of f-MWCNTs solution (1.5 mg $mL^{-1}$) was added dropwise under vigorous stirring at room temperature to the GO solution. The mixture was left overnight to precipitate the self-assembled product and then collected by centrifugation (8000 rpm). The viscous mixture was freeze-dried for 72 h to obtain a dry powder.

### Fabrication of pristine PLA and PLA/f-MWCNTs/GO composite membranes

In this study, all membranes were prepared using the non-solvent-induced phase inversion method (Supplementary Fig. 2). Table 1 shows the compositions of the dope solutions, the nanomaterial content, and the amount of PLA used for the membrane fabrication. First, PLA pellets and the self-assembled positively charged nanomaterial of f-MWCNTs/GO were dried overnight in an oven at a temperature of 70 °C to ensure the removal of any moisture traces. The f-MWCNTs/GO nanohybrid with different concentrations (1.5, 3, and 6 wt%) were added to the DMAc, then placed in Branson® Ultrasonic Bath for 3 h to assure dispersity in the solvent. In the previous solution, known masses of PLA and PVP were then added and stirred for 24 h at 70 °C to form a homogeneous solution. Before membrane casting, all solutions were sonicated for at least an hour, then placed in a vacuum oven at 70 °C for another hour and finally placed on the shelf for 30 min to achieve bubble-free solutions. Lastly, the membranes were cast on DMAc-wetted support on the glass plate using a casting knife set with a thickness of 250 microns. The wet membranes were then immediately immersed in a deionized (DI) water coagulation bath for 24 h, the membranes were again rinsed with DI water to remove any traces of DMAc and finally left to dry and stored at room temperature. Moreover, the fabrication of free-standing membranes was performed because some characterizations required the membranes to be without support.

### Filtration performance of fabricated membranes

The performance of the prepared membranes was assessed by measuring the water permeability and the removal of nutrients using a vacuum filtration set-up. First, the synthetic wastewater was prepared by dissolving the known masses of each salt of ammonium chloride ($NH_4Cl$) and potassium dihydrogen phosphate ($KH_2PO_4$) in two separate glass vials containing DI water, while stirring at room temperature. Synthetic wastewaters were prepared to have final concentrations of $NH_4^+$-N and $PO_4^{3-}$-P, similar to typical municipal wastewater[2,82] of 30.1 ± 0.8 and 10.2 ± 0.6 mg $L^{-1}$, respectively. A few drops of 0.1 M HCL and 0.1 M NaOH solutions were added to adjust the pH to 7, if necessary. The membranes were cut into an area of 12.6 $cm^2$ and kept in DI water for 15 min prior to the performance tests. The set-up was set at a pressure of 0.8 bar and the membranes were placed in the set-up. To compact the membrane, DI water was left to pass through the membrane for the first 10 min. Then, the water flux measurements (J; L $m^{-2}$ $h^{-1}$) (Eq. (5)) were recorded for an hour every 15, 30, 45, and 60 min and an average value was recorded.

$$J = \frac{V}{A \times t} \quad (5)$$

where *V*, *A*, and *t* represent the volume of permeate (L), the membrane's effective area ($m^2$), and the time (h). Synthetic wastewater was then filtered through the membrane and the permeate was collected after 30 min to measure the concentrations of $NH_4^+$-N and $PO_4^{3-}$-P, using a HACH spectrophotometer (DR3900 LANGE HACH, Germany). Consequently, the nutrient removal performance (*R*; %) (Eq. (6))[78] of the membranes was calculated as follows:

$$\text{Removal}(\%) = \frac{C_F - C_P}{C_F} \times 100 \quad (6)$$

where $C_F$, and $C_P$ are the concentrations (mg $L^{-1}$) of the nutrient before and after filtration, respectively.

Static adsorption experiments were carried out on the fabricated membranes in addition to the dynamic filtration experiments. The membranes were cut into 9 $cm^2$ pieces and submerged in a 50 mL bottle containing the synthetic wastewater prepared for 24 h. The bottles were placed in a shaker operating at 100 rpm to reach the adsorption equilibrium. Similarly, the concentrations of nutrients before and after the experiment were measured using a spectrophotometer, and the amount of adsorbed nutrient ions ($q_e$) on the membrane was calculated using Eq. (7):

$$q_e(g^{-1}) = \frac{(C_F - C_P) \times V}{M} \quad (7)$$

where $V$ is the volume of solution used (L), and $M$ is the mass of the membrane (g).

Lastly, four cycles of filtration experiments were carried out using raw wastewater to investigate the reusability of the fabricated membranes. The membranes were cleaned by rinsing them with DI water multiple times after each raw wastewater filtration cycle. Then the water flux was measured to investigate the durability of the membranes.

### Reporting summary

Further information on research design is available in the Nature Research Reporting Summary linked to this article.

## DATA AVAILABILITY

All data generated or analysed during this study are included in this published article and its supplementary information files.

Received: 2 July 2022; Accepted: 20 October 2022;
Published online: 30 October 2022

## REFERENCES

1. Tosun, İ. Ammonium removal from aqueous solutions by clinoptilolite: determination of isotherm and thermodynamic parameters and comparison of kinetics by the double exponential model and conventional kinetic models. *Int. J. Environ. Res. Public Health* **9**, 970 (2012).
2. Yildiz, E. Phosphate removal from water by fly ash using crossflow microfiltration. *Sep. Purif. Technol.* **35**, 241–252 (2004).
3. Yang, H., Liu, J., Hu, P., Zou, L. & Li, Y. Y. Carbon source and phosphorus recovery from iron-enhanced primary sludge via anaerobic fermentation and sulfate reduction: performance and future application. *Bioresour. Technol.* **294**, 122174 (2019).
4. Wang, L., Pan, G., Shi, W., Wang, Z. & Zhang, H. Manipulating nutrient limitation using modified local soils: a case study at Lake Taihu (China). *Water Res.* **101**, 25–35 (2016).
5. Taddeo, R., Prajapati, S. & Lepistö, R. Optimizing ammonium adsorption on natural zeolite for wastewaters with high loads of ammonium and solids. *J. Porous Mater.* **24**, 1545–1554 (2017).
6. Chen, P. et al. Utilization of municipal solid and liquid wastes for bioenergy and bioproducts production. *Bioresour. Technol.* **215**, 163–172 (2016).
7. Peyravi, M., Jahanshahi, M., Alimoradi, M. & Ganjian, E. Old landfill leachate treatment through multistage process: membrane adsorption bioreactor and nanofitration. *Bioprocess Biosyst. Eng.* **39**, 1803–1816 (2016).
8. Omar, H. & Rohani, S. Treatment of landfill waste, leachate and landfill gas: a review. *Front. Chem. Sci. Eng.* **9**, 15–32 (2016).
9. Mandowara, A. & Bhattacharya, P. K. Simulation studies of ammonia removal from water in a membrane contactor under liquid-liquid extraction mode. *J. Environ. Manag.* **92**, 121–130 (2011).
10. Moradihamedani, P. & Abdullah, A. H. Preparation and characterization of polysulfone/zeolite mixed matrix membranes for removal of lowconcentration ammonia from aquaculture wastewater. *Water Sci. Technol.* **77**, 346–354 (2018).
11. Ahmadiannamini, P., Eswaranandam, S., Wickramasinghe, R. & Qian, X. Mixed-matrix membranes for efficient ammonium removal from wastewaters. *J. Memb. Sci.* **526**, 147–155 (2017).
12. Jorgensen, T. C. & Weatherley, L. R. Ammonia removal from wastewater by ion exchange in the presence of organic contaminants. *Water Res.* **37**, 1723–1728 (2003).
13. Wilsenach, J. A., Schuurbiers, C. A. H. & van Loosdrecht, M. C. M. Phosphate and potassium recovery from source separated urine through struvite precipitation. *Water Res.* **41**, 458–466 (2007).
14. ER, C., CK, B. & S, L. Characterizing and contrasting the microbial ecology of laboratory and full-scale EBPR systems cultured on synthetic and real wastewaters. *Water Res.* **108**, 124–136 (2017).
15. Moradihamedani, P. Recent developments in membrane technology for the elimination of ammonia from wastewater: a review. *Polym. Bull.* **78**, 5399–5425 (2020).
16. Bódalo, A., Gómez, J. L., Gómez, E., León, G. & Tejera, M. Ammonium removal from aqueous solutions by reverse osmosis using cellulose acetate membranes. *Desalination* **184**, 149–155 (2005).
17. Adam, M. R. et al. Current trends and future prospects of ammonia removal in wastewater: a comprehensive review on adsorptive membrane development. *Sep. Purif. Technol.* **213**, 114–132 (2019).
18. Prochnow, L. I., Kiehl, J. C., Pismel, F. S. & Corrente, J. E. Controlling ammonia losses during manure composting with the addition of phosphogypsum and simple superphosphate. *Sci. Agric.* **52**, 346–349 (1995).
19. Seruga, P. et al. Removal of ammonia from the municipal waste treatment effluents using natural minerals. *Molecules* **24**, 3633 (2019).
20. Rohani, R. et al. Ammonia removal from raw water by using adsorptive membrane filtration process. *Sep. Purif. Technol.* **270**, 118757 (2021).
21. Spears, B. M. et al. Geo-engineering in lakes: a crisis of confidence? *Environ. Sci. Technol.* **48**, 9977–9979 (2014).
22. Xie, J. et al. Removal and recovery of phosphate from water by lanthanum hydroxide materials. *Chem. Eng. J.* **254**, 163–170 (2014).
23. Zong, E. et al. Adsorptive removal of phosphate ions from aqueous solution using zirconia-functionalized graphite oxide. *Chem. Eng. J.* **221**, 193–203 (2013).
24. Xia, W. J. et al. Phosphorus removal from diluted wastewaters using a La/C nanocomposite-doped membrane with adsorption-filtration dual functions. *Chem. Eng. J.* **405**, 126924 (2021).
25. Ahmad, A. F. et al. Biodegradable poly (lactic acid)/poly (ethylene glycol) reinforced multi-walled carbon nanotube nanocomposite fabrication, characterization, properties, and applications. *Polymers* **12**, 1–22 (2020).
26. Intrchom, W., Roy, S. & Mitra, S. Functionalized carbon nanotube immobilized membrane for low temperature ammonia removal via membrane distillation. *Sep. Purif. Technol.* **235**, 116188 (2020).
27. Ibrahim, Y. et al. Surface modification of anti-fouling novel cellulose/graphene oxide (GO) nanosheets (NS) microfiltration membranes for seawater desalination applications. *J. Chem. Technol.* **95**, 1915–1925 (2020).
28. Junaidi, N. F. D. et al. Effect of graphene oxide (GO) on the surface morphology & hydrophilicity of polyethersulfone (PES). *IOP Conf. Ser. Mater. Sci. Eng.* **358**, 012047 (2018).
29. Wang, Z. et al. Novel GO-blended PVDF ultrafiltration membranes. *Desalination* **299**, 50–54 (2012).
30. Mohamad, S. N. K. et al. Evaluation on structural properties and performances of graphene oxide incorporated into chitosan/poly-lactic acid composites: Cs/pla versus cs/pla-go. *Polymers* **13**, 1839 (2021).
31. Wu, J. K. et al. Synergistic effects of CNT and GO on enhancing mechanical properties and separation performance of polyelectrolyte complex membranes. *Mater. Des.* **119**, 38–46 (2017).
32. Shafiei Amrei, S., Asghari, M., Esfahanian, M. & Zahraei, Z. Highly selective carbon nanotube-coupled graphene oxide-incorporated polydimethylsiloxane membrane for pervaporative membrane bioreactor ethanol production. *J. Chem. Technol.* **95**, 1604–1613 (2020).
33. Zhuo, Y., Liu, J., Li, Q., Qiu, B. & Xing, G. Preparation and characterization of WPU/CNT/GO nanocomposites. *Integr. Ferroelectr.* **171**, 52–58 (2016).
34. Zhang, Y. et al. Building a highly stable ultrathin nanoporous layer assisted by glucose for desalination. *Engineering* **16**, 247–255 (2022).
35. Torres, A., Li, S. M., Roussos, S. & Vert, M. Poly(lactic acid) degradation in soil or under controlled conditions. *J. Appl. Polym. Sci.* **62**, 2295–2302 (1996).
36. Xiong, Z. et al. Robust superhydrophilic polylactide (PLA) membranes with a TiO2 nano-particle inlaid surface for oil/water separation. *J. Mater. Chem. A. Mater.* **5**, 6538–6545 (2017).
37. Minbu, H. et al. Preparation of poly(L-lactic acid) microfiltration membranes by a nonsolvent-induced phase separation method with the aid of surfactants. *J. Memb. Sci.* **479**, 85–94 (2015).

38. Khalil, H. et al. Asymmetrical ultrafiltration membranes based on polylactic acid for the removal of organic substances from wastewater. *J. Water Process. Eng.* **45**, 102510 (2022).
39. Nassar, L. et al. Development of green polylactic acid asymmetric ultrafiltration membranes for nutrient removal. *Sci. Total Environ.* **824**, 153869 (2022).
40. Kashi, S., Gupta, R. K., Baum, T., Kao, N. & Bhattacharya, S. N. Dielectric properties and electromagnetic interference shielding effectiveness of graphene-based biodegradable nanocomposites. *Mater. Des.* **109**, 68–78 (2016).
41. Jin, S. H., Yoon, K. H., Park, Y.-B. & Bang, D. S. Properties of surface-modified multiwalled carbon nanotube filled poly(ethylene terephthalate) composite films. *J. Appl. Polym. Sci.* **107**, 1163–1168 (2008).
42. Datsyuk, V. et al. Chemical oxidation of multiwalled carbon nanotubes. *Carbon N. Y* **46**, 833–840 (2008).
43. Bera, M., Chandravati, Gupta, P. & Maji, P. K. Facile one-pot synthesis of graphene oxide by sonication assisted mechanochemical approach and its surface chemistry. *J. Nanosci. Nanotechnol.* **18**, 902–912 (2018).
44. Ahmed, D. S., Haider, A. J. & Mohammad, M. R. Comparesion of functionalization of multi-walled carbon nanotubes treated by oil olive and nitric acid and their characterization. *Energy Procedia* **36**, 1111–1118 (2013).
45. Abdullah, M. P. & Zulkepli, S. A. The functionalization and characterization of multi-walled carbon nanotubes (MWCNTs). *AIP Conf. Proc.* **1678**, 50033 (2015).
46. Lee, D. W. et al. Highly controllable transparent and conducting thin films using layer-by-layer assembly of oppositely charged reduced graphene oxides. *J. Mater. Chem.* **21**, 3438–3442 (2011).
47. Wojciechowski, K. & Klodzinska, E. Zeta potential study of biodegradable antimicrobial polymers. *Colloids Surf. A. Physicochem. Eng. Asp.* **483**, 204–208 (2015).
48. Massoumi, B., Mohammad, R., Mojtaba, R. & Mehdi, A. Amine - functionalized carbon nanotubes as curing agent for polystyrene - modified novolac epoxy resin: synthesis, characterization and possible applications. *Appl. Phys. A* **125**, 1–7 (2019).
49. Huang, L. et al. Core–shell SiO2@RGO hybrids for epoxy composites with low percolation threshold and enhanced hermos-mechanical properties. *J. Mater. Chem. A. Mater.* **2**, 18246–18255 (2014).
50. Jafarizad, A. et al. PEGylated graphene oxide/Fe3O4site: synthesis, characterization, and evaluation of its performance as de novo drug delivery nanosystem. *Biomed. Mater. Eng.* **29**, 177–190 (2018).
51. Li, B., Liu, T., Hu, L., Wang, Y. & Nie, S. Facile preparation and adjustable thermal property of stearic acid-graphene oxide composite as shape-stabilized phase change material. *Chem. Eng. J.* **215–216**, 819–826 (2013).
52. Dube, S. T., Moutloali, R. M. & Malinga, S. P. Hyperbranched polyethyleneimine/multi-walled carbon nanotubes polyethersulfone membrane incorporated with Fe-Cu bimetallic nanoparticles for water treatment. *J. Environ. Chem. Eng.* **8**, 103962 (2020).
53. He, X., Xu, X., Bo, G. & Yan, Y. Studies on the effects of different multiwalled carbon nanotube functionalization techniques on the properties of bio-based hybrid non-isocyanate polyurethane. *RSC Adv.* **10**, 2180–2190 (2020).
54. Wulandari, S. A., Arifin, Widiyandari, H. & Subagio, A. Synthesis and characterization carboxyl functionalized multi-walled carbon nanotubes (MWCNT-COOH) and NH2 functionalized multi-walled carbon nanotubes (MWCNTNH2). *J. Phys. Conf. Ser.* **1025** (2018).
55. Xu, D., Tan, X., Chen, C. & Wang, X. Removal of Pb(II) from aqueous solution by oxidized multiwalled carbon nanotubes. *J. Hazard Mater.* **154**, 407–416 (2008).
56. Guo, J. et al. Unravelling intercalation-regulated nanoconfinement for durably ultrafast sieving graphene oxide membranes. *J. Memb. Sci.* **619**, 118791 (2021).
57. Gao, X., Jang, J. & Nagase, S. Hydrazine and thermal reduction of graphene oxide: reaction mechanisms, product structures, and reaction design. *J. Phys. Chem. C.* **114**, 832–842 (2010).
58. Hsiao, M. C. et al. Preparation of covalently functionalized graphene using residual oxygen-containing functional groups. *ACS Appl. Mater. Interfaces* **2**, 3092–3099 (2010).
59. Ai, L. et al. Removal of methylene blue from aqueous solution with magnetite loaded multi-wall carbon nanotube: kinetic, isotherm and mechanism analysis. *J. Hazard Mater.* **198**, 282–290 (2011).
60. Wang, X. et al. Formation of unique three-dimensional interpenetrating network structure with a ternary composite. *J. Mater. Sci. Mater. Electron.* **29**, 18699–18707 (2018).
61. Sun, M., Wang, G., Li, X., Cheng, Q. & Li, C. Interfacial synthesis and supercapacitive performance of hierarchical sulfonated carbon nanotubes/polyaniline nanocomposites. *Ind. Eng. Chem. Res.* **51**, 3981–3987 (2012).
62. Jian, M. Q., Xie, H. H., Xia, K. L. & Zhang, Y. Y. Challenge and opportunities of carbon nanotubes. *Ind. Appl. Carbon Nanotubes* 433–476 (2017).
63. Makhetha, T. A. & Moutloali, R. M. Incorporation of a novel Ag–Cu@ZIF-8@GO nanocomposite into polyethersulfone membrane for fouling and bacterial resistance. *J. Memb. Sci.* **618**, 118733 (2021).
64. Sianipar, M., Kim, S. H., Khoiruddin, Iskandar, F. & Wenten, I. G. Functionalized carbon nanotube (CNT) membrane: progress and challenges. *RSC Adv.* **7**, 51175–51198 (2017).
65. Wang, R., Zhao, X., Lan, Y., Liu, L. & Gao, C. In situ metal-polyphenol interfacial assembly tailored superwetting PES/SPES/MPN membranes for oil-in-water emulsion separation. *J. Memb. Sci.* **615**, 118566 (2020).
66. Ibrahim, Y., Naddeo, V., Banat, F. & Hasan, S. W. Preparation of novel polyvinylidene fluoride (PVDF)-Tin(IV) oxide (SnO2) ion exchange mixed matrix membranes for the removal of heavy metals from aqueous solutions. *Sep. Purif. Technol.* **250**, 117250 (2020).
67. Kumar, M. & Ulbricht, M. Novel antifouling positively charged hybrid ultrafiltration membranes for protein separation based on blends of carboxylated carbon nanotubes and aminated poly(arylene ether sulfone). *J. Memb. Sci.* **448**, 62–73 (2013).
68. Ghalamchi, L., Aber, S., Vatanpour, V. & Kian, M. A novel antibacterial mixed matrixed PES membrane fabricated from embedding aminated Ag3PO4/g-C3N4 nanocomposite for use in the membrane bioreactor. *J. Ind. Eng. Chem.* **70**, 412–426 (2019).
69. Yu, L. et al. Preparation and characterization of HPEI-GO/PES ultrafiltration membrane with antifouling and antibacterial properties. *J. Memb. Sci.* **447**, 452–462 (2013).
70. Chieng, B. W., Ibrahim, N. A., Yunus, W. M. Z. W. & Hussein, M. Z. Poly(lactic acid)/poly(ethylene glycol) polymer nanocomposites: Effects of graphene nanoplatelets. *Polymers* **6**, 93–104 (2014).
71. Zhu, S. et al. Preparation and characterization of a polyethersulfone/polyaniline nanocomposite membrane for ultrafiltration and as a substrate for a gas separation membrane. *RSC Adv.* **5**, 27211–27223 (2015).
72. Vuković, G. D. et al. Removal of cadmium from aqueous solutions by oxidized and ethylenediamine-functionalized multi-walled carbon nanotubes. *Chem. Eng. J.* **157**, 238–248 (2010).
73. Khanghahi, B., Shokri, E., Esmizadeh, E., Shojaei, S. & Etemadi, H. Preparation of PVC / PLA ultrafiltration membrane with enhanced structural properties. *IChEC* (2020).
74. Yoon, Y., Kye, H., Yang, W. S. & Kang, J.-W. Comparing graphene oxide and reduced graphene oxide as blending materials for polysulfone and polyvinylidene difluoride membranes. *Appl. Sci.* **10**, 2015 (2020).
75. Lim, M. Z. Y., Chong, W. C., Lau, W. J. & Koo, C. H. Performance of thin film composite membranes for ammonium removal and reuse of ammonium-enriched solution for plant growth. *Water Supply* **21**, 318–330 (2021).
76. He, Y., Lin, H., Dong, Y., Liu, Q. & Wang, L. Simultaneous removal of ammonium and phosphate by alkaline-activated and lanthanum-impregnated zeolite. *Chemosphere* **164**, 387–395 (2016).
77. Mohamed, A. et al. Removal of chromium (VI) from aqueous solutions using surface modified composite nanofibers. *J. Colloid Interface Sci.* **505**, 682–691 (2017).
78. Adam, M. R. et al. Impact of sintering temperature and pH of feed solution on adsorptive removal of ammonia from wastewater using clinoptilolite based hollow fibre ceramic membrane. *J. Water Process. Eng.* **33**, 101063 (2020).
79. Wimalasiri, Y., Mossad, M. & Zou, L. Thermodynamics and kinetics of adsorption of ammonium ions by graphene laminate electrodes in capacitive deionization. *Desalination* **357**, 178–188 (2015).
80. Mohammadi, R., Hezarjaribi, M., Ramasamy, D. L., Sillanpää, M. & Pihlajamäki, A. Application of a novel biochar adsorbent and membrane to the selective separation of phosphate from phosphate-rich wastewaters. *Chem. Eng. J.* **407**, 126494 (2021).
81. Abdullah, N. et al. Polysulfone/hydrous ferric oxide ultrafiltration mixed matrix membrane: preparation, characterization and its adsorptive removal of lead (II) from aqueous solution. *Chem. Eng. J.* **289**, 28–37 (2016).
82. Hammer, Sr. & Hammer, Jr. *Water and Wastewater Technology* (Pearson, 2013).

## ACKNOWLEDGEMENTS

The authors acknowledge the financial support received from Khalifa University of Science and Technology (KU) in Abu Dhabi (UAE) (Award No. CIRA-2020-107). Furthermore, the authors thank the Center for Membranes and Advanced Water Technology (CMAT) (Award No. RC2-2018-009) at KU for the support.

## AUTHOR CONTRIBUTIONS

L.N.: Conceptualization, methodology, and writing the original draft. V.S.W. and H.M.H.: Methodology, review and editing. H.K., F.B., and V.N.: Review and editing. S.W.H.: Conceptualization, validation, resources, supervision, review and editing, and administration.

## COMPETING INTERESTS

The authors declare no competing interests.

## ADDITIONAL INFORMATION

**Supplementary information** The online version contains supplementary material available at https://doi.org/10.1038/s41545-022-00206-w.

**Correspondence** and requests for materials should be addressed to Shadi W. Hasan.

**Reprints and permission information** is available at http://www.nature.com/reprints

**Publisher's note** Springer Nature remains neutral with regard to jurisdictional claims in published maps and institutional affiliations.